Vertical Spin Tunnel Testing and Stability Analysis of Multi-Mission Earth Entry Vehicles

Louis J Glaab[1]

Eugene A. Morelli[2]

C. Michael Fremaux[3]

Jacob Bean[4]

[1]Mail Stop 489, NASA LaRC, Hampton, VA, 23681, louis.j.glaab@nasa.gov

[2]Mail Stop 308, NASA LaRC, Hampton, VA, 23681, e.a.morelli@nasa.gov

[3]Mail Stop 308, NASA LaRC, Hampton, VA, 23681, charles.m.fremaux@nasa.gov

[3]National Institute of Aerospace, Hampton, VA, 23681, jacob.j.bean@nasa.gov

ABSTRACT

Multi-Mission Earth Entry Vehicles (MMEEVs) are blunt-body vehicles designed with the purpose of transporting payloads from space to the surface of Earth. To achieve high reliability and minimum weight, MMEEVs avoid using limited-reliability systems, such as parachutes, retro-rockets, and reaction control systems. Multi-Mission Earth Entry vehicles rely on the natural aerodynamic stability of the vehicle throughout the Entry, Descent, and Landing phase of flight.

Testing in NASA Langley's 20-FT Vertical Spin Tunnel (20-FT VST) was conducted to improve subsonic aerodynamic models for this class of vehicle. As the center of mass of a vehicle moves aft, due to placement of components or other design aspects, vehicle stability is decreased, resulting in larger amplitude oscillations and reduced ability to recover from atmospheric disturbances such as turbulence.

Design requirements for effective impact attenuation involve maximum attitude limits at landing. In addition, mission reliability requirements establish the minimum capability of the vehicle to recover from atmospheric disturbances. The objectives of the 20-FT VST testing were to define usable subsonic center of mass limits to meet potential design requirements, and aerodynamic parameters for 6-degree-of-freedom simulations, for a range of MMEEV designs. This report documents the resulting data from the 20-FT VST testing for an array of 60-deg sphere-cone MMEEVs. Model configurations included in the test matrix were 1.2 meter and 1.8 meter designs. The addition of a backshell extender, which resulted in a 150% increase in backshell diameter for the 1.2 meter design, provided a third test configuration. Data were acquired for unperturbed tethered, perturbed tethered, and unperturbed and untethered test methods. Center of Gravity limits were established for all MMEEV configurations. System Identification (SID) methods were used to determine the aerodynamic models for the MMEEV configurations in order to provide databases for subsequent 6-degree-of-freedom simulations, as well as to validate stability criteria. Results indicate that adequate data was obtained from the 20-FT VST testing to support SID analysis.

1. SYMBOLS AND ACRONYMS

6-DOF	6-degree-of-freedom
$\dot{\alpha}$	Time rate of change of angle of attack
α	Angle of attack
$\dot{\beta}$	Time rate of change of sideslip
β	Angle of sideslip
C_A	Axial force coefficient
C_l	Rolling moment coefficient
C_m	Pitching moment coefficient
C_n	Yawing moment coefficient
C_N	Normal force coefficient
C_Y	Side force coefficient
CM	Center of Mass
D	Model and Full-Scale diameter
I_{XX}	Model moment inertia about X axis
I_{YY}	Model moment inertia about Y axis
I_{ZZ}	Model moment inertia about Z axis
l_m	Model length
l_v	Full-scale vehicle length
MMEEV	Multi-Mission Earth Entry Vehicle
M-SAPE	Multi-Mission System Analysis for Planetary Entry tool
MSPS	Model Space Positioning System
MSR	Mars Sample Return
N	Ratio of model to full-scale size
OML	Outer Mold Line
P	Pterturbed
$\dot{p}$	Non-dimensional roll rate
$\hat{q}$	Non-dimensional pitch rate
$\hat{r}$	Non-dimensional yaw rate
R_e	Reynolds number
Rx, Ry,	Euler angles (x-y-z rotation sequence)

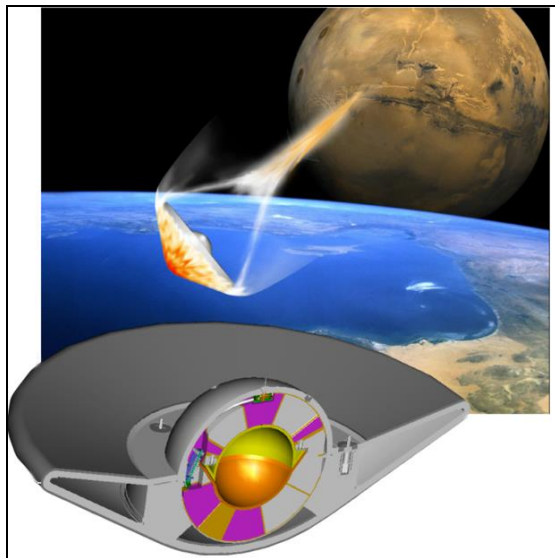|	
Rz	
ρ_m	Model air density
ρ_V	Full scale vehicle air density
SID	System IDentification methods
T	Tethered
TPS	Thermal Protection System
UT	Un-Tethered
ν_m	Model velocity
ν_v	Full scale vehicle velocity
V_∞	Model total airspeed
VST	NASA LaRC Vertical Spin Tunnel
ψ, θ, ϕ	Standard aerospace Euler angles (z-y-x rotation sequence)
x, y, z	Wind tunnel model axis system
X, Y, Z	VST axis system

2. INTRODUCTION

Figure 1 – Mars Sample Return concept

Multi-Mission Earth Entry Vehicles (MMEEVs) are designed to transport payloads from outside of the atmosphere to the surface of the Earth. They serve as the last leg of missions to gather samples from around the solar system for detailed analysis on Earth. Multi-Mission Earth Entry Vehicles can have various sizes, shapes, designs, and concept of operations that reflect unique mission requirements. In general, however, many of the prior and planned future MMEEVs can be viewed as a class of vehicle with many similar characteristics. Multi-Mission Earth Entry Vehicles have high speeds resulting from direct atmospheric entries at interplanetary speeds. In addition, many MMEEVs are single-stage entry concepts that do not include parachutes, retro-rockets, or reaction control systems for example, in order to minimize complexity and weight while maximizing reliability. At landing the kinetic energy is dissipated by built-in energy absorption systems as described in [Reference 1] to protect the payload. Figure 1 illustrates a NASA-LaRC con-

cept for a Mars Sample Return (MSR) Earth Entry Vehicle, which is considered to be a member of the family of MMEEVs.

To assess vehicle designs for multiple missions, as well as develop advanced integrated multi-disciplinary automated design tools, the Multi-Mission Systems Analysis for Planetary Entry (M-SAPE) tool [Reference 2] is being developed. It is used to facilitate the design of MMEEVs for an array of missions and develop and visualize the trade space. The M-SAPE tool improves and speeds up the design activities such as trade studies, sensitivity analyses, Monte Carlo analyses, and vehicle optimization. The trade space limits being developed for M-SAPE includes vehicle diameters from 0.9 to 1.8 meters with payloads from 5 to 25 kg.

During the final minutes of descent, MMEEVs will be flying at subsonic Mach conditions. Shapes designed to optimize aerothermal heating, such as large angle blunted cones, can possess limited usable center-of-gravity (CG) ranges due to subsonic static and dynamic aerodynamic stability issues [Reference 3]. Depending on the mission, payload mass and density, entry trajectory, and payload impact and temperature requirements, MMEEVs can have varying overall diameters and backshell sizes which can also affect stability.

The M-SAPE program requires a data base to support its system engineering functions and adequately model vehicle dynamics for a range of MMEEV designs. For low-fidelity analyses, an approximate range of usable CGs for a family of MMEEVs designs is required. Higher-fidelity 6-degree-of-freedom (6-DOF) simulation analyses require more comprehensive aerodynamic databases. Existing aerodynamic models used for M-SAPE are based on a combination of computational fluid dynamics and documented and un-documented wind-tunnel data for similar entry vehicles. Results from [References 4] combined with dynamic aerodynamic data obtained from the Viking program [Reference 5] were used as the basis for the existing subsonic aerodynamic models in M-SAPE.

The objectives of the current effort were to: 1) provide a comprehensive low-speed aerodynamic database for a range of 60-deg Sphere-Cone MMEEVs for use with the M-SAPE tool, 2) provide additional data for blunt-body entry vehicles. Model configurations tested included 1.2 meter and 1.8 meter MMEEVs designs. The addition of a backshell extender, which resulted in a 150% increase in the backshell diameter for the 1.2 meter design, provided a third test configuration. Center of Gravity limits were established based on the test results that are applicable to 60-deg sphere-cone MMEEV configurations over the range of conditions tested. Aerodynamic System IDentification (SID) tools [Reference 6] were used to determine the aerodynamic models for 6-degree-of-freedom simulations. The test technique employed herein has some significant strengths compared to other traditional wind-tunnel and flight-test techniques. These strengths are: 1) negligible sting support interference issues due to the free-flying nature of the test in the 20-FT Vertical Spin Tunnel (VST), 2) actual dynamic motions of the vehicle that are not constrained due to model support limits, and 3) large amount of dynamic oscillation data (compared to actual flight testing) that can be acquired in a controlled environment. Re-

sults indicate that adequate data was obtained from the 20-FT VST testing to support SID analysis.

3. METHOD

3.1. Multi-Mission Earth Entry Vehicles Tested

In order to accomplish the test objectives, a series of MMEEVs were designed using M-SAPE. Dynamically-scaled models of these designs were subsequently fabricated and tested in the NASA LaRC 20-FT VST. All MMEEVs were designed for a 12 km/sec entry velocity using a Phenolic Impregnated Carbon Ablator (PICA) Thermal Protection System (TPS). The 1.8m MMEEV with 25 kg payload is considered to define the upper limit of size and payload of the MMEEV family of vehicles. The 1.2m MMEEV with 15 kg payload is more representative of the median size design for this class of vehicles. Selection of two different size vehicles, with different payloads, provided a range of vehicle size, shape of back shell, and mass characteristics to use in the modeling process. The back shell extender (BSE) used with the 1.2m MMEEV provided a direct evaluation of the effect of this outer mold line (OML) change.

Table 1 Full-Scale Vehicle Parameters

Parameter	MMEEV Configuration		
	1.8m	1.2m	1.2m+BSE
Surface Area (m^2)	2.54	1.13	1.13
Nose Radius (/D)	0.173	0.183	0.183
Shoulder Radium (/D)	0.029	0.03	0.03
Payload (kg)	25	15	15
TPS	PICA	PICA	PICA
Total Vehicle Mass (kg)	83	44	44
I_{xx}(kg-m^2)	21.6	4.4	3.9
I_{yy}(kg-m^2)	12.5	2.6	3.0
I_{zz}(kg-m^2)	12.4	2.6	3.0

3.2. Model Scaling

Definition of the required model scale characteristics were based on the methods in [Reference 7]. For this scaling process, Froude number and relative density similitude are required between model and vehicle to obtain dynamic similarity. Dynamic similarity is required in order to apply the model angular rates and motion to the full-scale vehicle. The scaling factors are provided in Table 2. The subscript "m" stands for model and "v" for full-scale vehicle. Atmospheric density is part of the scaling process. For 20-FT VST testing, the air density was assumed to be standard sea-level atmospheric conditions (i.e. 1.225 kg/m^3) and the full-scale vehicle air density was assumed to be 1.055 kg/m^3, which corresponds to the 5,000 ft elevation of the intended landing site in the Utah Test and Training Range.

Table 2 Model Scaling Factors

Parameter	Scale Factor (Model/Full-Scale)
Linear Dimension	$N = \ell_m / \ell_v$

Relative Density	1
Froude Number	1
Mass	$N^3 \rho_m/\rho_v$
Moment of Inertia	$N^5 \rho_m/\rho_v$
Linear Velocity	$N^{1/2}$
Linear Acceleration	1
Angular Velocity	$1/N^{1/2}$
Time	$N^{1/2}$
Reynolds Number	$N^{3/2} \nu_m/\nu_v$

3.3. Wind-Tunnel Models Tested

The models were constructed using polycarbonate material and manufactured using an additive manufacturing process. For this manufacturing process, the models were essentially "printed" from a machine using 3-D design software that enabled the designer to meet OML as well as model mass characteristic requirements. Once removed from the additive manufacturing machine, the models required some sanding and painting. The reflective targets were then added and their locations were precisely measured with respect to the model reference point. Figure 2 is a photograph of the 1.8m MMEEV model that shows the placement of the reflective targets that were essential to track model flight during testing.

Figure 2 – Forebody of the 1.8m MMEEV

Model scaling factors and mass characteristics for the three MMEEV configurations are provided in Table 3. Also included in Table 3 is the Δ_{x-VA} term which is the distance from the surface of the vehicle to the theoretical apex. For testing in the 20-FT VST, ~1 ft diameter (0.3048 m) models are the preferred size. This size provides adequate separation for the reflective targets and sufficient internal volume to accommodate most ballast conditions. One foot diameter models also provide adequate room in the 20-FT VST to accommodate dynamic movement of the vehicle during testing. For this test series, the 1.8m MMEEV model had a diameter of 1 ft (0.3048m). The diameter for the 1.2m and 1.2m+BSE models was 11.8" (0.3m). Given the differences in full-scale vehicle size, the scaling factor for the 1.8m was

different from the 1.2m and 1.2m+BSE MMEEV configurations, as shown in Table 3.

Figures 3, 4, and 5 are backshell photographs of the 1.8m, 1.2m, and 1.2m+BSE MMEEV configurations tested. Note that reflective targets were not applied to the aft of these vehicles. Figure 3 also shows some external ballast applied in order to achieve a high-inertia mass condition. As can be seen in Figures 3, 4, and 5, the size of the backshell compared to the rest of the model is the smallest for the 1.8m MMEEV and increases for the 1.2m and is the largest for the 1.2m+BSE configuration. Note that the forward surface of the vehicle at the centerline is used as the reference point for the CG location reported herein. The positive x axis is pointing forward.

Table 3 Model Mass Characteristics CG=0.214/D

Parameter	MMEEV Configuration		
	1.8m	1.2m	1.2m+BSE
Scaling factor	0.169	0.25	0.25
D (m)	0.3048	0.3	0.3
Mass (kg)	0.473	0.809	0.813
I_{xx} (kg-m^2)	0.003456	0.004939	0.004455
I_{yy} (kg-m^2)	0.002005	0.002914	0.003408
I_{zz} (kg-m^2)	0.001990	0.002914	0.003439
Δ_{X-VA} (m)	0.0081	0.0085	0.0085

Figure 3 – Backshell of the 1.8m MMEEV

Figure 4 – Backshell of the 1.2m MMEEV

Figure 5 – Backshell of the 1.2m+BSE MMEEV

3.4. Wind Tunnel

The dynamic stability tests were performed in the Langley 20-FT VST which is a sea-level atmospheric, low-speed, annular return tunnel with a closed, twelve-sided test section that is 6.1m (20 ft) wide and 7.6m (25 ft) long. The maximum tunnel dynamic pressure is approximately 431 Pa (9 lb/ft^2) at a speed of 26.5 m/s (87 ft/s) which corresponds to a Reynolds number of 1.8x10^6 per meter (550,000 per ft). For this test, the average dynamic pressure was approximately 77 Pa for the 1.8m MMEEV. Dynamic pressure increased to 118 Pa for the 1.2m and 1.2m+BSE configurations due to the higher model weight. The resulting Reynolds number based on model maximum diameter was approximately 0.24x10^6 and 0.29x10^6 for the 1.8m and 1.2m MMEEV configurations, respectively. The fan drive control is designed to provide rapid 4.6 m/s^2 acceleration and -7.6 m/s^2 deceleration of the flow (+15 ft/s^2 and -25 ft/s^2, respectively) through a joystick controller so that a model may be kept vertically in the designated test volume. A lightweight "safety tether" system is used to minimize model damage due to impact with the test-section walls and reduce test time when appropriate. The safety tether length is controlled by a heavy-duty electronic fishing reel, and can secure the model within several seconds after recovery is initiated. See Figure 6 for a cross sectional sketch of the facility. The test section walls are also padded to further mitigate model damage due to impact. The tether consists of a lightweight braided nylon line attached to the model with a ball-bearing swivel and was kept slack during data runs. Upper and lower nets prevent models from getting drawn into the fan or falling through the flow straightening honeycomb.

A method to excite or perturb the models is also part of the 20-FT VST test capability. Essentially the perturbation method is a long pole with a padded end. One of the tunnel operators can contact the model with the perturbation pole to induce model responses. A usable model perturbation was one that exceeded the nominal limit cycle oscillations while not immediately tumbling the vehicle. A trial-and-error approach was used to determine appropriate perturbations for the tests.

A series of cameras around the test section provided video coverage as input to an optical data acquisition system (to be discussed in the next section). The 20-FT VST has been used for studying the spin characteristics of aircraft (hence the

name of the tunnel), however, there have also been numerous dynamic stability tests for atmospheric entry vehicles. Among the entry vehicles tested are Mercury [8], Gemini [9], Apollo [10], Pioneer Venus [11] and Stardust [12].
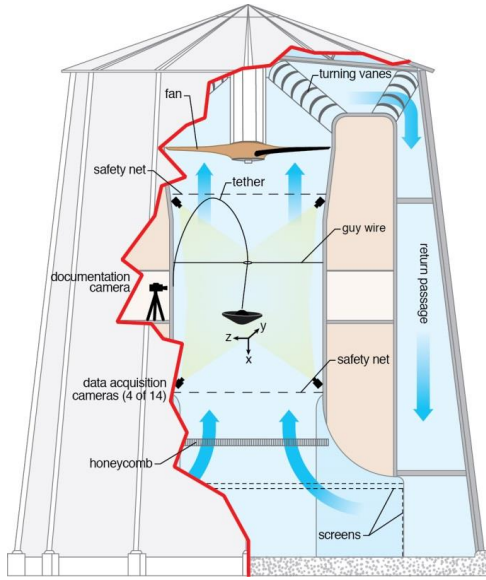

Figure 6 – NASA LaRC 20-FT Vertical Spin Tunnel

3.5. Data Acquisition System

An optical data acquisition system was used to obtain 6-DOF motion time histories of models during dynamic tests. The 20-FT VST Model Space Positioning System, or MSPS [13], is a non-intrusive, workstation-based system that has eight digital cameras to image a pattern of retro-reflective targets on a model. It is used to generate post-test estimates of model attitude (ψ, θ, ϕ) and spatial position (X, Y, Z) with respect to an earth-fixed test section axis system (Figure 6) at a sample rate of 150 Hz, using near-infrared LEDs as a light source. During data acquisition, test section states (dynamic pressure, flow velocity, temperature) are recorded on a separate system and time-correlated for post-test processing. Comparisons to a reference at known attitudes indicate that angles reported by MSPS are accurate to within ±0.2 degrees.

The wind-tunnel model mass characteristics were measured using a Space Electronics model KSR330-6 mass properties machine. Measurement of the inertias was accurate to within 0.1% and CG location to within +/-0.0005" (~0.00004/D) as stated by the manufacturer.

Video of every test run was acquired using a high-definition camera. Before the start of each run, a computer screen was configured to display the wind-tunnel name, project, test block, and run numbers, along with other descriptive data. The video operator recorded the parameters displayed on the computer screen prior to test initiation.

3.6. Experimental Matrix

Testing in the 20-FT VST was performed in blocks of runs for two separate test series. One series of tests were con-

ducted in 2010 and focused on the 1.8m MMEEV over a narrower range of CGs and inertias. A complementary test series was conducted in 2013 that added two additional MMEEV configurations (1.2m and 1.2m+BSE) and additional CG locations for the 1.8m MMEEV.

At least three repeat runs of a specific test condition were included in each block. Test techniques employed were: tethered (T) or untethered (UT), perturbed (P) or unperturbed (UP). No untethered perturbed testing was conducted. Blocks of data were acquired for specific combinations of model configuration (i.e. 1.8m, 1.2m, or 1.2m+BSE), mass characteristics (i.e. CG and inertias), and type of test performed (i.e., tethered unperturbed, tethered perturbed, or untethered unperturbed). The test condition is defined for specific combinations of model configuration and mass characteristics. For most tethered model conditions, unperturbed and perturbed data were acquired. No perturbed testing was performed for test conditions that had departures in unperturbed testing. A departure is defined as increasing oscillation amplitudes that exceed ~60 degrees. The CG positions of the models were moved aft until the vehicle was not stable during unperturbed testing. In this context, an unstable configuration was one where at least one of the repeat runs exhibited a departure. The 1.8m MMEEV was only tested to a 0.25 CG/D location because this model configuration was unable to move the CG any further aft while still mostly enclosing the ballast and preserving the outer model line. The definitions of each block of runs, along with the numbers of runs in each block, are listed in Table 4. Data blocks 1 through 7 were performed in 2010. All other data blocks were completed in 2013.

Table 4 Experimental Test Matrix

TC	Blocks	OML	CG	Inertias	Test Series
1	1,2,7	1.8m	0.214D	Nominal	T-UP, T-P, UT-UP
2	3,4	1.8m	0.234D	Nominal	T-UP, T-P
3	5,6	1.8m	0.234D	1.5*Nom	T-UP,T-P
4	8,9	1.8m	0.250D	Nominal	T-UP,T-P
5	10,11,23	1.2m	0.214D	Nominal	T-UP, T-P, UT-UP
6	21,22	1.2m	0.234D	Nominal	T-UP, T-P
7	12	1.2m	0.250D	Nominal	T-UP
8	13,14-15,30	1.2m+BSE	0.214D	Nominal	T-UP, T-P, UT-UP
9	19,20	1.2m+BSE	0.234D	Nominal	T-UP, T-P
10	16,17	1.2m+BSE	0.250D	Nominal	T-UP, T-P
11	18	1.2m+BSE	0.257D	Nominal	T-UP
1	25,26,28	1.8m	0.214D	Nominal	T-UP, T-P ,UT-UP

3.7. Model Mass Characteristics

Figure 7 illustrates the average of the two lateral components of inertia (i.e. I_{yy}, I_{zz}) as a function of CG for the three MMEEV configurations tested. The 150% inertia condition

for the 1.8m MMEEV is also included in Figure 7. All inertias are relative to the body axis with the origin at the CG. Results in Figure 7 also indicate that the inertia variations were limited to approximately 10% across the CGs tested. Required CG location was to within +/-0.001D.
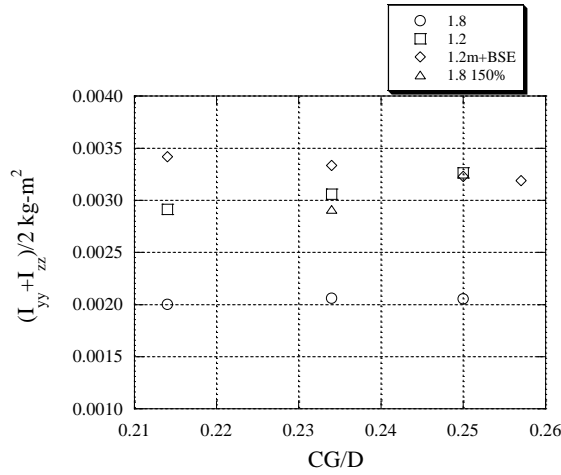

Figure 7 – Inertias tested

3.8. Test Method

Tethered unperturbed testing was initiated with the model at rest near the bottom of the test section supported by the safety tether with the wind tunnel off. Video and the MSPS were started and confirmed to be working. Gradually, the wind-tunnel was brought up to speed and model would begin to "fly". Stabilization of the wind-tunnel was performed over approximately 30 seconds and the model was stable in roughly in the middle of test section. Once the model was stabilized, the wind-tunnel operator would start data recording. The model was allowed to oscillate in the tunnel for at least approximately 45 seconds for each unperturbed run. After 45 seconds of data were acquired, the wind-tunnel was gradually stopped and the model would then hang on the end of the tether. Tethered, unperturbed testing was performed for a range of mass characteristics with the CGs gradually moved aft until departures occurred.

For perturbed testing, the same start-up process was used as unperturbed tethered testing. Once the model was stable and data were being recorded, a wind-tunnel technician would attempt to perturb the model using a long pole with a pad at the end. Data were acquired for approximately 45 seconds after the model was successfully perturbed and was able to recover to steady-state oscillations. Then, the wind-tunnel was then gradually shut-down and the model would hang on the end of the tether. Approximately one successful perturbation was generated for 3 attempts. A successful perturbation was one where the model would be perturbed to have larger oscillations than steady-state (approximately 20 to 70 degrees) and not immediately tumble.

Untethered testing was performed with the wind-tunnel and video systems already operating. Once the wind-tunnel was stabilized at the desired velocity a wind-tunnel technician would gently release the model into the test section. Once the model was successfully stabilized in the test section, the data recording would be initiated. If the model travelled close to the wind-tunnel walls (i.e. within ~1 ft) the data recording would be stopped and the model would be gently repositioned in the test section using long poles and subsequently released. Data recording would then be resumed. Untethered runs would acquire approximately 30 seconds of data, which was considered to be the smallest amount of data needed for the SID analyses. The length of the untethered runs were limited by the amount of time the model would remain within the test section before it moved too close to the walls. As was the case for the tethered perturbed testing, multiple attempts were needed for each adequate data run. At the end of an untethered block of testing, the model would be retrieved from the test section, again using long poles, or the wind-tunnel would be gradually stopped with the model gently falling into the netting at the bottom of the test section for subsequent manual retrieval.

Model mass characteristics were established for each test condition. Technicians placed ballast in the models to achieve the desired CGs and moments of inertia. Models mass characteristics would then be measured as described previously. If the mass characteristics were not within acceptable limits, the model was re-ballasted and the mass measurement process repeated.

Overall, the wind-tunnel test generated 193 data runs for 11 different test conditions shown in Table 4.

4. DATA ANALYSIS

System IDentification (SID) techniques as described in [Reference 6] were applied in an effort to identify aerodynamic models for use in 6-DOF simulations. System identification is defined as the determination, on the basis of observation of input and output, of a system within a specified class of systems to which the system under test is equivalent [6]. For the SID analysis performed herein, the Systems IDentification Programs for AirCraft (SIDPAC) tool set was used [6]. This commercially available tool set provides an array of highly useful MATLAB programs specifically designed for SID analysis.

For the SID analysis, time, model position (X, Y, and Z), model orientation (R_x, R_y, and R_z), and model mass characteristics (M, I_{xx}, I_{yy}, I_{zz}) were used along with wind-tunnel velocity (V_∞). Density was assumed to be standard atmospheric conditions. Model orientation angles, R_x, R_y, and R_z, are Euler angles by definition, however, the sequence of rotation is altered (i.e., X-Y-Z rotation sequence) to avoid singularities associated with the nearly vertical flight path experienced with 20-FT VST testing. The first step in the SID process is to smooth the resulting wind-tunnel time series X, Y, Z and R_x, R_y, and R_z data and convert all the data into consistent metric units. Smoothing is especially important since one and two time derivatives of the time series data were required to define linear and angular velocities and accelerations. For this step, the SMOO function from SIDPAC was used with a 3 Hz cut-off frequency. The SIDPAC DERIV function was used to compute smoothed linear and angular rates and accelerations.

The next step in the SID process was to calculate the experimental nondimensional force (C_A, C_N, C_Y) and moment (C_m, C_n, C_l) coefficients, along with the angle of attack, α, angle of sideslip, β, and the time derivative of angle of attack and sideslip, $\dot{\alpha}$, $\dot{\beta}$, as a function of time.

Identification of the aerodynamic force and moment coefficient models was accomplished using several SIDPAC tools. The MOF function was used to identify specific model terms (i.e., α, β, α^3, β^3, $\hat{q}$, $\hat{r}$) to use for the model equations. Results from this process indicated that the experimental forces and moments were dominated by α and β. Body rates $\hat{q}$ and $\hat{r}$ only accounted for approximately 2% of the overall variation in the aerodynamic coefficients. Nonlinear aerodynamic terms (α^3, β^3) were included to accommodate nonlinear effects in the higher angle of attack range (i.e. >15 degs). The resulting modelling equations are provided here. The C_0 constant terms for all the equations, except for C_A, were included to account for data system biases that could potentially result from flow angularities, model manufacturing asymmetries, etc. An analysis and comparison of $\dot{\alpha}$ and q was performed and the two quantities were found to be nearly identical. As a result their average was used for the nondimensional pitch rate. A similar analysis and results were obtained for r and $-\dot{\beta}$. The reference length for the calculations was the model diameter, D.

Axial Force, C_A:

$$C_A = C_{A_0} \cos(\alpha) \qquad (1)$$

Normal Force, C_N:

$$C_N = C_{N_0} + C_{N_\alpha} \alpha + C_{N_{\alpha^3}} \alpha^3 \qquad (2)$$

Side Force, C_Y:

$$C_Y = C_{Y_0} + C_{Y_\beta} \beta + C_{Y_{\beta^3}} \beta^3 \qquad (3)$$

Pitching moment, C_m:

$$C_m = C_{m_0} + C_{m_\alpha} \alpha + C_{m_{\alpha^3}} \alpha^3 + C_{m_q} \hat{q} \qquad (4)$$

Yawing moment, C_n:

$$C_n = C_{n_0} + C_{n_\beta} \beta + C_{n_{\beta^3}} \beta^3 + C_{n_r} \hat{r} \qquad (5)$$

Rolling moment, C_l:

$$C_l = C_{l_0} + C_{l_p} \hat{p} \qquad (6)$$

Where:

$$\hat{q} = \left(\frac{q+\dot{\alpha}}{2}\right) * D/(2*V_\infty) \qquad (7)$$

$$\hat{r} = \left(\frac{r+\dot{\beta}}{2}\right) * D/(2*V_\infty) \qquad (8)$$

$$\hat{p} = p * D/(2*V_\infty) \qquad (9)$$

The equations listed above were used along with the SIDPAC LESQ function. Results from this determined the unknown model parameters (i.e. C_{m_α}, C_{n_β}, etc). The SIDPAC function R_COLORES was used to calculate the covariance matrix for the parameters. The standard error was then calculated from the square root of the diagonal of the covariance matrix. Signal-to-noise ratios were calculated using SIDPAC SMOO for the time series data.

During the results and discussion sections, determining if two sets of data produced similar results was performed simply through inspection of the standard error bars. If the standard error bars overlapped from one set of data to the next, then those two sets of results were considered to be in statistical agreement. If the standard error bars did not overlap, then the results were considered to be statistically different. The standard error bars represent 95 percent confidence intervals (±2 standard errors), centered at the model parameter estimate.

5. RESULTS AND DISCUSSION

5.1. Signal-to-Noise Ratios, Coefficient of Determination, and Evaluation of SID Modelling

The signal-to-noise ratios (SNRs) were evaluated for all the nondimensional aerodynamic coefficients in an effort to assess the potential to apply SID techniques. The results from this analysis indicated that for C_A and C_l the SNRs were too low to extract meaningful models from the data (SNR<1). In order to extract usable aerodynamic parameters from the data, a minimum amount of information needs to be embodied in the data. For the MMEEV testing, very little, if any, data was available for the C_l parameter estimation due to the lack of motion of the vehicle in this axis. In general, the model did not oscillate in roll which would have been required for data analysis and modelling for this axis. As a result, the C_l parameter is neglected. For C_A, the motion of the vehicle, knowledge of the instantaneous velocity at the model, and/or the resolution of the MSPS was insufficient to support the SID analysis. For C_A, the mean value (constant term only) was used for the results for the different test conditions and configurations.

Data were analysed using separate lateral and normal axes. Proceeding in this manner permits independent calculation of coefficients for these axes. Taking advantage of vehicle symmetry affords a check on the data analysis process. For example, the magnitudes of the normal and side forces should be equal. Similarly, the magnitudes of the pitching yawing moments should also be equal. Pitch and yaw damping should be equal to each other. These checks were used as part of the data validation process.

Results for the coefficient of determination (R^2) were calculated to demonstrate the overall capability of the modelling applied to the data. The R^2 metric quantifies the amount of variation explained by the model compared to the total variation. Table 5 shows the R^2 values for the two force (C_N, C_Y) and moment (C_m, C_n) coefficients that were modelled for all data runs longer than 15 seconds (98 total runs). Table 5

also provides the SNR for the experimental data. From Table 5 it can be seen that a large amount of the variation in the aerodynamic coefficient data was being modelled. The differences in the level of model fit between the force and moment coefficients likely involve the overall motion of the vehicle during testing. In general, the wind-tunnel models oscillated about the normal and lateral axes. The reflective targets mounted near the edge of the vehicles exhibited a large amount of vertical motion and as a result likely facilitated the estimation of angular attitudes. Lateral motions of the vehicle were much smaller which likely contributed to the lesser R^2 results for C_N and C_Y.

Figures 8, and 9 provide comparisons of the experimental data with the resulting model data from the SID analysis for the pitching moment amd normal force coefficients, respectively. The data in Figures 8 and 9 were taken from Block 1, Run 1 which is for the 1.8m MMEEV at CG=0.214/D location. The specific values of R^2 for this run where 0.88 and 0.89 for the pitch moment and normal force coefficients, respectively. From these figures, it can be seen that the modelled results agree well with the experimental data.

Table 5 Coefficient of Determination R^2 for all data runs>15 seconds long

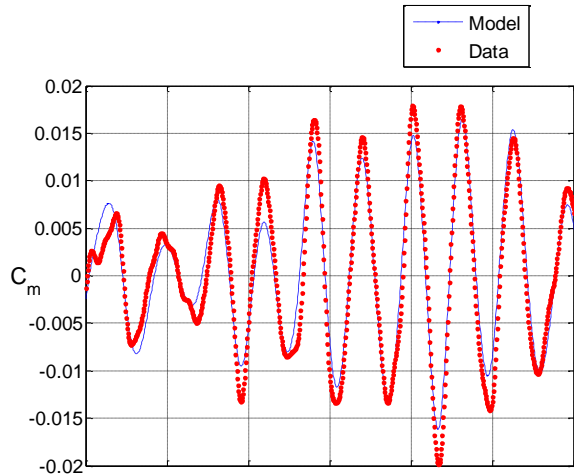|	C_N	C_Y	C_m	C_n
Average R^2	0.85	0.84	0.94	0.94
Average SNR	9.7	9.5	9.2	8.2

Figure 8 - Example comparison of experimental and modelled pitching moment coefficient
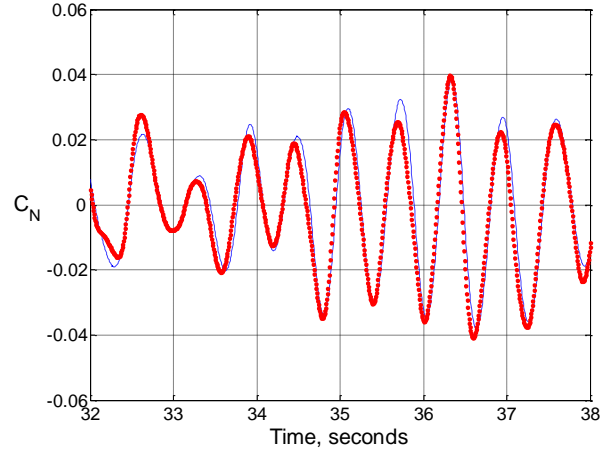

Figure 9 – Example comparison of experimental and modelled normal force coefficient

Unlike the coefficient of determination, R^2, which describes the capability of the modeling equations to characterize the existing data, the standard error is used to describe the uncertainty in the estimates of the individual model parameters used in those equations. The standard error for the parameters included in equations 2 through 5 were determined using the R_COLORES function in SIDPAC, which computes the parameter covariance matrix accounting for colored residuals, see [Reference 6].

The standard errors for each parameter from equations 2 to 5, except for the constant terms, are provided in Table 6 for the force equations and Tables 7 and 8 for the moment equations, for all data runs that were longer than 15 seconds (98 runs total). From these two tables it can be seen that the standard error ranged from a low of 2.7% for the static stability terms (i.e., C_{m_α}, C_{n_β}) up to a high of 968% for the nonlinear component of the side force equation. Overall, the moment coefficients were associated with lower standard errors, which is consistent with the coefficient of determination discussion provided previously. The nonlinear components of the equations experienced very high standard errors due to the range of oscillations for the varous test conditions. For the forward CG locations, the vehicles would oscillate at lower angles of attach (i.e. <10 degs) with mostly linear aerodynamics. It was only for the aft CG locations, with oscillations >15 degs, where some non-linear aerodynamic effects were generated. Note that the damping terms (C_{m_q}, C_{n_r}) had standard errors of approximately 32%. The damping parameters are considered high-priority aerodynamic terms required for stability analysis and simulation and were included in the modeling equations even though they had a relatively small effect.

Table 6 Standard error for the force equation coefficients

Force coeffi-cients	C_{N_α}	$C_{N_{\alpha^3}}$	C_{Y_β}	$C_{Y_{\beta}3}$
Average error	0.0331	0.7667	0.0341	0.7530
Average coeffi-cients	0.2626	0.2507	-0.2665	-0.0778
% error	12.6	305	12.8	968

Table 7 Standard error for the pitching moment equation coefficients

Moment coefficients	C_{m_α}	$C_{m_{\alpha^3}}$	C_{m_q}
Average error	0.0034	0.1593	0.0172
Average coefficient	-0.1259	0.0894	-0.0529
% error	2.7	178	32.5

Table 8 Standard error for the yawing moment equation coefficients

Moment coefficients	C_{n_β}	$C_{n_{\beta^3}}$	C_{n_r}
Average error	0.0035	0.1749	0.0177
Average coefficient	0.1287	-0.1629	-0.0559
% error	2.7	107	31.7

5.2. Effect of CG on Total Angle of Attack

During this testing the CG location of the MMEEV models was varied and moved aft until the model was no longer stable for unperturbed testing. The 1.8m MMEEV never became unstable over the range of CGs tested for the baseline inertia condition. Note that the aft CG location limit for the 1.8m MMEEV was 0.250/D due to ballast limits. The 1.2m MMEEV became unstable at 0.250 D CG. The addition of the backshell extender enabled the 1.2m+BSE configuration to be stable at a CG location of 0.250 /D CG but unstable at 0.257/D CG. As the CG was moved aft, the oscillations grew in amplitude. Figure 10 illustrates the rms total angle of attack for each MMEEV configuration over a range of CGs. Note that the CG locations have been slightly adjusted for this plot for clarity for the 0.214/D, 0.234/D, and 0.250/D locations. The solid symbols represent the maximum total angle of attack for each test condition. From Figure 10 it can be seen that all MMEEVs experienced increased oscillations as the CG was moved aft. The 1.8m MMEEV with the baseline inertias had the lowest range of oscillations for the configurations tested. Increasing the inertias for the 1.8m MMEEV to 150% of baseline approximately doubled the rms total angle of attack at the 0.234/D CG location. The 1.2m MMEEV had the highest oscillations for the baseline inertia condition.

Of the configurations tested, departures were observed for the 1.8m MMEEV with 150% inertias at 0.234/D, the 1.2m MMEEV at 0.250/D, and the 1.2m+BSE at 0.257/D, CG locations. From Figure 10 it can be seen that these 3 unstable configurations had rms total angle of attack oscillations of 14 degrees (for the 1.8m+150% inertia and 1.2m configurations) and 15.5 degrees for the 1.2m+BSE configuration. Also note that maximum oscillations for these 3 configurations exceeded 25 degrees. The maximum total angle of attack oscillation for the stable configurations was approximately 24 degrees.

Figure 10 – RMS total angle of attack as a function of CG location.

5.3. Effect of CG on Pitching Moment

Pitching and yawing moment air flow angle derivatives as a function of CG and configuration are presented in Figure 11 along with the ±2 standard error bars. Note that CG locations are measured from the surface of the vehicle and not the virtual cone apex. From Figure 11, it can be seen that the 1.8m MMEEV configuration had significantly lower pitching and yawing moment derivatives than the other two configurations over all of the CG locations tested. This difference could be due to the smaller nose radius of the 1.8m MMEEV or the different backshell configurations. The difference in shoulder radius across the three configurations is considered to be very small (i.e. 0.029 D compared to 0.030 D) and not likely to produce significant changes in the aerodynamics of the vehicle. Moving the CG aft also produced significant differences in the pitching and yawing moment air flow angle derivatives (which represent static stability), as anticipated. However, significant differences due to CG location are evident only between the extreme aft locations, for the 1.8m and 1.2m+BSE configurations. Very little, if any change in pitching and yawing moment static stability is evident for the 1.2m configuration across the CG locations tested.
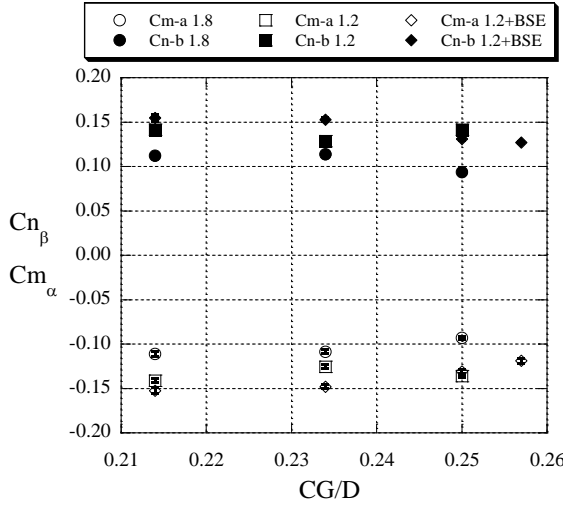
Figure 11 – Linear pitching and yawing moment coefficients as a function of CG location.

5.4. Effect of CG on Dynamic Stability

Pitching and yawing moment dynamic stability derivatives as a function of CG and configuration are presented in Figure 12 along with the ±2 standard error bars. The 0.214/D, 0.234/D, and 0.25/D CG locations were slightly adjusted for the 1.8m and 1.2+BSE configurations in this plot, for clarity. As can be seen from Figure 12, pitch and yaw damping coefficients were not significantly affected by CG location and corresponding range of oscillations, or configuration. The results in Figure 12 also indicate that all the data for the forward CG location of 0.214/D were nearly identical for all configurations tested. The largest, yet insignificant, variation in the data was observed for the mid CG location of 0.234/D where damping varied from ~-0.04 for the 1.8m up to ~-0.07 for the 1.2+BSE configurations. A slight decrease was observed for the results for the 1.2m+BSE configuration at the most aft CG location of 0.257/D. The lack of effect from CG location on pitch and yaw damping support the linear modelling of the dynamic stability. If the aerodynamic damping was significantly affected by the oscillation amplitude, then a variation in the damping coefficients would have been anticipated for the different CG locations. Results presented in Figure 12 suggest that the damping parameters are unaffected by oscillation amplitude over the conditions tested. Because the damping estimates are in statistical agreement, it is possible to obtain a more accurate estimate by averaging the parameter estimates, with weighting determined by their standard error. The consistency in the damping for pitch and yaw motions, which would be expected physically, gives confidence in the data analysis and modeling methods.
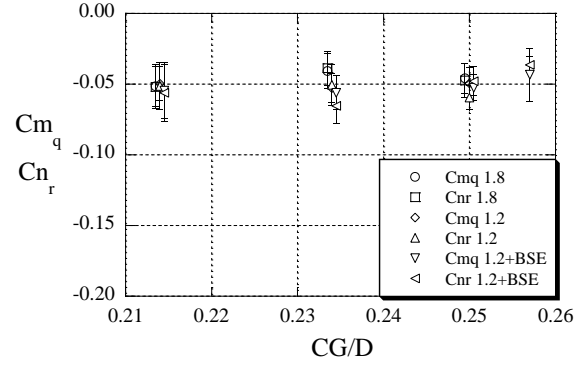

Figure 12 – Linear dynamic pitch and yaw damping coefficients as a function of CG location.

5.5. CG Limits

Based upon the observed results from the current test a CG limit is established. Results from Reference 3 and 14 indicate that the a vehicle's required pitch damping can be estimated as a function of the vehicle's mass characterstic term and the slope of the lift coefficient (i.e. $(\frac{2I}{mD^2})^{C_{L_\infty}}$). Results from the limit CG testing conducted herein can used along with the mass characteristic term to establish a range of usable CGs. Proceeding in this manner provides an ability to account for changes in the vehicle's mass properties over the ranges tested. Figure 13 illustrates the results from this analysis of the data. Given the small amount of CG limit data acquired, the results provided in Figure 13 are considered approximate and only represent a method of estimating the aft CG limit for 60-degree sphere-cone models similar to those tested as part of this study. More data is needed to more fully populate the model mass characteristic range of results.
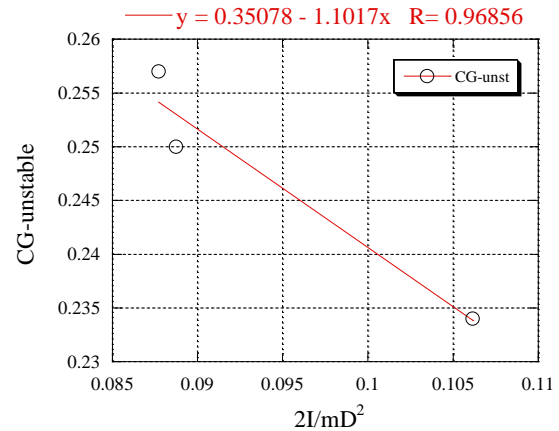

Figure 13 – Unstable CG locations vs. model mass characteristics.

6. SUMMARY

A series of 60-deg sphere-cone Multi-Mission Earth Entry Vehicle (MMEEVs) designs were successfully tested in the NASA LaRC 20-FT Vertical Spin Tunnel (20-FT VST). The objectives of the 20-FT VST testing were to define usable subsonic center of mass limits to meet potential design requirements, and determine aerodynamic parameters for 6-degree-of-freedom simulations, for a range of MMEEV designs. Testing was performed over a range of center of gravity (CG) locations and inertias for a series of MMEEVs.

Data analyses included the application of System IDentification (SID) techniques that provided the capability to determine aerodynamic models and uncertainties from the wind-tunnel data time histories. Standard error results from the SID analyses indicated that the static moment parameters were known to within 2.7%, static force parameters to with ~13%, and damping parameters to within ~33%. This level of modelling accuracy, which was a function of the test instrumentation and the experimental method used, is considered adequate to meet the test objectives.

All configurations tested exhibited increased oscillation amplitudes as the CG locations were moved aft or the inertia was increased. The most stable configuration was the 1.8m which was stable and provided good recovery from perturbations for all CG locations tested for the baseline inertias. A 150% inertia increase caused the 1.8m configuration to become unstable at the CG=0.234/D CG location.

No effects of configuration or CG were observed for normal force, side force, or pitch and yaw damping parameters. A significant difference due to configuration was observed for pitch and yaw moment static stability terms ($C_{m_\alpha}, and\ C_{n_\beta}$). The 1.8m configuration had significantly lower static stability than the other two configurations tested. This result could be due to the sharper nose radius or the much smaller backshell of the 1.8m configuration. The expected variation due to CG location was evident in the static stability terms.

Future plans include publication of a NASA Technical Paper to fully document the results acquired herein.

7. REFERENCES

1. Mitcheltree, R.; Hughes, S.; Dillman, R.; Teter J.: *An Earth Entry Vehicle for Returning Samples from Mars,* 2nd International Symposium on Atmospheric Reentry Vehicles and Systems, Arcachon France, 2001.

2. Samareh, J. A., Maddock, R. W., and Winski, R. G., *An Integrated Tool for System Analysis of Sample Return Vehicles*, 2012 IEEE Aerospace Conference, Big Sky, Montana, March 3-10, 2012.

3. Mitcheltree, R.; Fremaux, C., Yates, Leslie: Subsonic Static and Dynamic Aerodynamics of Blunt Entry Vehicles, AIAA 99-1020.

4. Marko, Wayne J.: Static Aerodynamic Characteristics of Three Blunted Sixty-Degree Half-Angle Cones at Mach Numbers From 0.6 to 1.3. NASA TR-32-1298.

5. Steinberg, S.: Experimental Pitch Damping Derivative for Candidate Viking Entry Configurations at Mach Numbers from 0.6 thru 3.0, June 1970, Martin Marrieta Corporation.

6. Klein, Vladislav and Morelli, Eugene A.: *Aircraft System Identification - Theory and Practice*. AIAA, Reston, VA, 2006.

7. Wolowicz, Chester H.; Bowman, James S.; Gilbert, William R.: *Similitude Requirements and Scaling Relationships as Applied to Model Testing*. NASA TP-1435, August, 1979.

8. Bowman, J. S., Dynamic Model Tests at Low Subsonic Speeds of Project Mercury Capsule Configurations with and without Drogue Parachutes, NASA TM X-459, 1961

9. Bowman, J. S., Dynamic-Model Investigation of a 1/20-Scale Gemini Spacecraft in the Langley Spin Tunnel, NASA TN-D-2191, 1964.

10. Lee, H. A., and Burk, S. M., Low-Speed Dynamic Model Investigation of Apollo Command Module Configurations in the Langley Spin Tunnel, NASA TND-3888, 1967

11. McCloy, R., Entry Dynamics Performance Predictions for Pioneer Venus Probes, AIAA-1978 1370, 1978.

12. Mitcheltree, R. A.; Fremaux, C. M.: *Subsonic Dynamics of Stardust Sample Return Capsule*. NASA TM-110329, 1997.

13. Snow, W. L., Childers, B. A., Jones, S. B., and Fremaux, C. M.: Recent Experiences with Implementing a Video Based Six Degree of Freedom Measurement System for Airplane Models in a 20-Foot Diameter Vertical Spin Tunnel, Proceedings of the SPIE Videometrics Conference, Vol. 1820, 1992, pp. 158-180.

14. Schoenenberger, Mark; Queen, Dr Eric M.: Limit Cycle Analysis Applied to the Oscillations of Decelerating Blunt-Body Entry Vehicles. NATO report 2008-18685.